Volume 17
Number 17
7 September 2024
Pages 6129–6422

# Energy & Environmental Science

rsc.li/ees

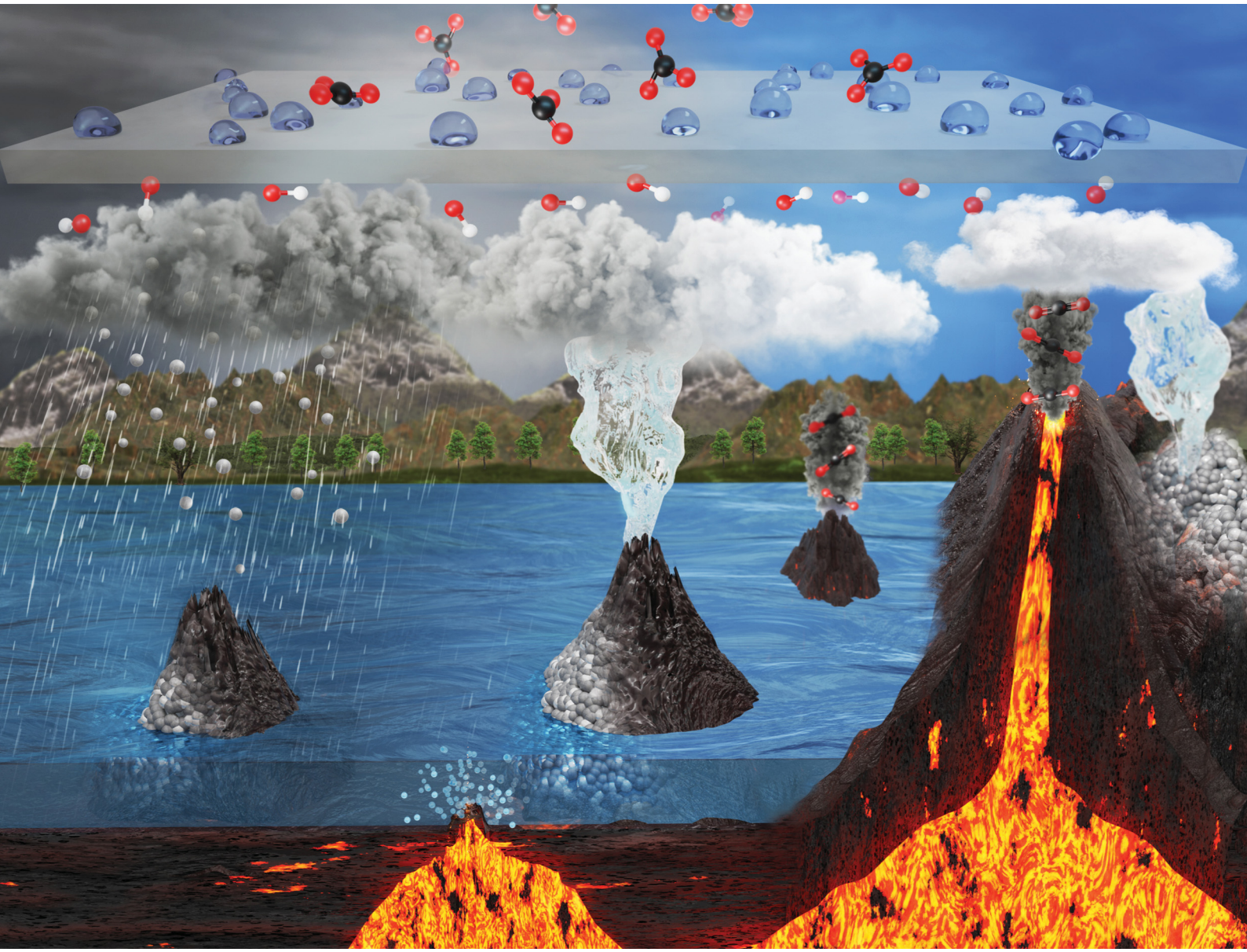

ISSN 1754-5706

ROYAL SOCIETY OF CHEMISTRY

**PAPER**

Woong Hee Lee, Hyung-Suk Oh *et al.*
Breaking the current limitation of electrochemical $CO_2$ reduction *via* a silica-hydroxide cycle

Energy & Environmental Science

ROYAL SOCIETY OF CHEMISTRY

PAPER

View Article Online
View Journal | View Issue

Check for updates

Cite this: *Energy Environ. Sci.*, 2024, **17**, 6215

# Breaking the current limitation of electrochemical $CO_2$ reduction *via* a silica-hydroxide cycle†

Chulwan Lim,‡[ab] Sangkuk Kim,‡[ac] Ji Hwan Song,‡[a] Man Ho Han,[a] Young-Jin Ko,[a] Kwan-Young Lee,[b] Jae-Young Choi,[de] Woong Hee Lee*[a] and Hyung-Suk Oh*[ade]

Received 28th January 2024,
Accepted 29th April 2024

DOI: 10.1039/d4ee00448e

rsc.li/ees

Alkaline local pH during a vigorous electrochemical $CO_2$ reduction reaction ($CO_2$RR) can improve the activity and selectivity of $CO_2$RR. However, it also leads to an alkalinity problem in that hydroxide ions obstruct the mass transfer of $CO_2$ to the active site, thereby limiting the current density. In this study, we introduce a silica-hydroxide cycle, which moderates the local pH by redistributing hydroxide ions, analogous to the carbonate-silicate cycle responsible for the drawdown of atmospheric $CO_2$ on Earth. In the membrane electrode assembly (MEA) of a $CO_2$ electrolyzer, $SiO_2$ undergoes weathering due to the high local pH and consequently consumes $OH^-$, reducing the pH within the MEA. The dissolved silicate ions move to the membrane and are almost regenerated to $SiO_2$ with release of $OH^-$. Geological and spectral observations suggest that the silica-hydroxide cycle reduces the local pH thereby enhancing mass transfer of $CO_2$, breaking the limitation of current density for $CO_2$RR. Our work proposes new chemical approaches to increase current density, mainly improved by physical methods, and contributes valuable insight for improving a variety of electrochemical systems.

Open Access Article. Published on 30 Apuli 2024. Downloaded on 11/02/2025 23:22:28.
This article is licensed under a Creative Commons Attribution-NonCommercial 3.0 Unported Licence.

**Broader context**

The electrochemical $CO_2$ reduction reaction ($CO_2$RR) is viewed as a promising approach to attain carbon neutrality while generating valuable fuels and chemicals. Enhancing the current density in $CO_2$RR presents a significant challenge for the efficient production of chemicals on a meaningful scale, which is essential for economic viability. Recently, various mechanical approaches have enhanced the performance of $CO_2$RR through enhancing the mass transfer of $CO_2$, playing a pivotal role in improving the current density. Nevertheless, in the high current density region, the hydroxide ions created during the reaction form a local alkaline environment, which converts $CO_2$ to carbonate ions, hindering the mass transfer of $CO_2$ to the catalyst surface and limiting the current density for $CO_2$RR. This study delves into the role of $SiO_2$ in the electrochemical $CO_2$RR regarding the silica-hydroxide cycle, which moderates the local pH by redistributing hydroxide ions. This mechanism draws a parallel with the silicate-carbonate cycle, which plays a crucial role in the natural sequestration of atmospheric $CO_2$ on Earth, thus offering a novel avenue for breaking the current density limitation of $CO_2$RR through controlled pH management.

## Introduction

The electrochemical $CO_2$ reduction reaction ($CO_2$RR) is viewed as a promising solution for achieving carbon neutrality while producing valuable fuels and chemicals.[1–3] Increasing the current density for $CO_2$RR poses a significant challenge for the mass production of chemicals while ensuring economic feasibility.[4,5] Recently, various mechanical approaches, including gas-phase $CO_2$, device design, gas diffusion electrode (GDE), membrane electrode assembly (MEA), pressurized system and nanosized catalyst, have successfully enhanced the performance of $CO_2$RR *via* enhancing mass transfer of $CO_2$, playing a pivotal role in improving the current density.[6–17] Under high current density regime coming from a recently developed system, an intriguing phenomenon, called local pH,

[a] *Clean Energy Research Center, Korea Institute of Science and Technology, Hwarang-ro 14-gil 5, Seongbuk-gu, Seoul 02792, Republic of Korea. E-mail: hyung-suk.oh@kist.re.kr, abcabac@kist.re.kr; Tel: +82 (0)2 958 5824*
[b] *Department of Chemical and Biological Engineering, Korea University, 145 Anam-ro, Seongbuk-gu, Seoul, 02841, Republic of Korea*
[c] *Hydrogen and Low-Carbon Energy R&D laboratories, POSCO HOLDINGS, 67 Cheongam-ro, Nam-gu, Pohang-si, Gyeongsangbuk-do, 37673, Republic of Korea*
[d] *School of Advanced Materials Science & Engineering, Sungkyunkwan University (SKKU), Suwon, 16419, Republic of Korea*
[e] *KIST-SKKU Carbon-Neutral Research Center, Sungkyunkwan University (SKKU), Suwon 16419, Republic of Korea*

† Electronic supplementary information (ESI) available. See DOI: https://doi.org/10.1039/d4ee00448e

‡ All authors contributed equally to this work.

Open Access Article. Published on 30 Apuli 2024. Downloaded on 11/02/2025 23:22:28.
This article is licensed under a Creative Commons Attribution-NonCommercial 3.0 Unported Licence.

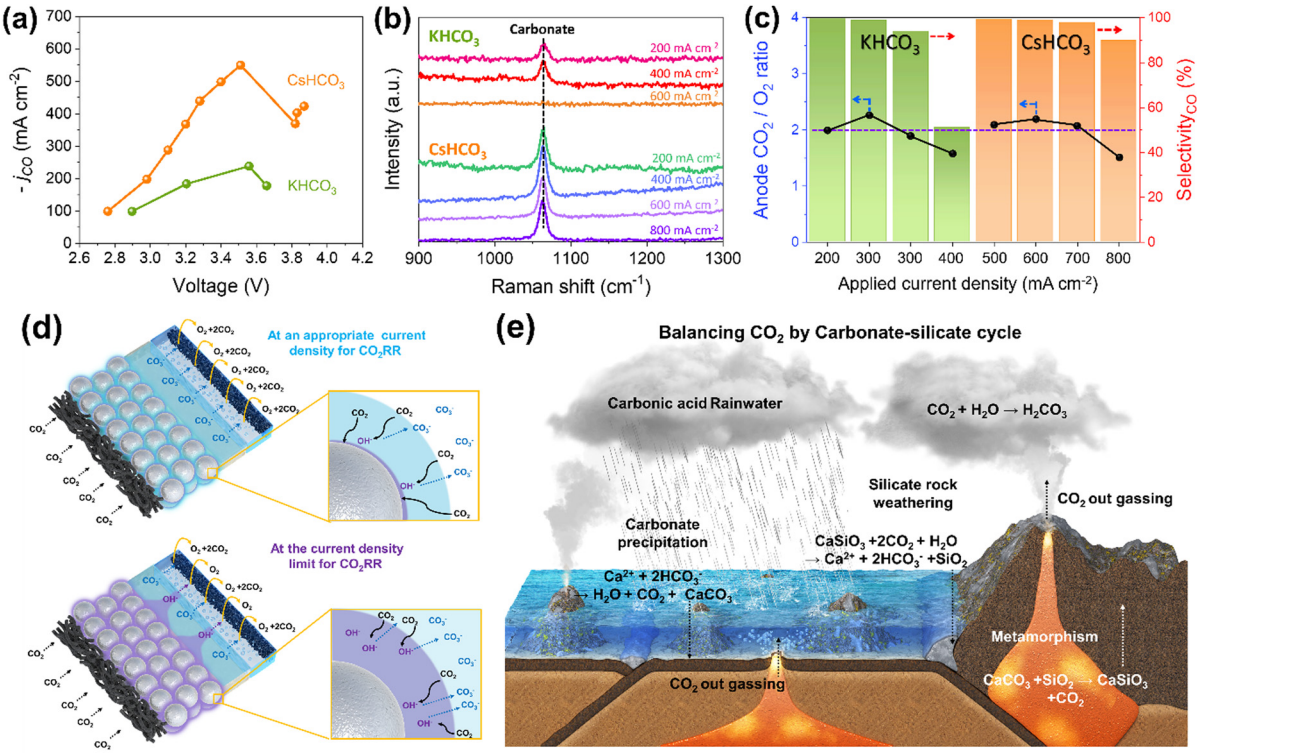


Fig. 1 Alkalinity issue in $CO_2$RR and carbonate-silicate cycle. (a) CO partial current density *versus* cell voltage in a zero-gap electrolyzer using Ag black with 0.1 M $KHCO_3$ and 0.1 M $CsHCO_3$. (b) *In situ*/*operando* Raman spectroscopy results with 1 M $KHCO_3$ and $CsHCO_3$ electrolytes. (c) $CO_2/O_2$ ratio at the anode in a zero-gap electrolyzer with 0.1 M $KHCO_3$ and 0.1 $CsHCO_3$. (d) A schematic depiction of the alkalinity problem in a zero-gap $CO_2$ electrolyzer. (e) A schematic representation of the carbonate-silicate geochemical cycle on Earth.

clearly appeared for $CO_2$RR. The hydroxide ions generated from the reaction create a local alkaline environment at the electrode, promoting $CO_2$RR *via* reducing the hydrogen evolution reaction (HER) and modulating binding energies for the intermediates.[18–24] Nevertheless, some studies addressing local pH have indicated an alkalinity problem in that hydroxide ions block the mass transfer of $CO_2$ to the catalyst by converting carbonate, limiting the current density for $CO_2$RR.[25,26] The alkalinity problem of $CO_2$RR can be validated using alkali cation effects. Numerous experimental and theoretical investigations reveal that a larger size of alkali cation exhibits smaller hydration number at the Helmholtz layer and lower p$K_a$ values near the electrode, mitigating the local pH phenomenon.[27–29] The current density of $CO_2$RR according to alkali cation was assessed in a $CO_2$ MEA electrolyzer using Ag black sprayed GDE (Fig. 1a and Fig. S1–S3, ESI†). $CsHCO_3$ electrolyte demonstrated a significantly higher maximum current density for $CO_2$RR than $KHCO_3$ electrolyte. To delve into the pH reaction environment of the cathode in the MEA electrolyzer, *in situ*/*operando* Raman spectroscopy and gas analysis of the anode were carried out (Fig. 1b and c). In the Raman spectra for the $KHCO_3$ electrolyte, the carbonate peak disappeared at current densities exceeding 400 mA $cm^{-2}$, while the carbonate peak persisted at a current density of 800 mA $cm^{-2}$ using $CsHCO_3$ electrolyte. The *in situ*/*operando* Raman spectroscopy focused on the catalyst surface. Thus, the disappeared carbonate peak indicates that the catalyst surface possesses high alkalinity with almost no carbonate ions resulting from reaction with $OH^-$ and $CO_2$ gas. These observations indicate that the larger size of Cs cations alleviates the local pH phenomenon at high current densities. The gas ratio of $CO_2$ and $O_2$ for the anode side decreased below 2 was observed at 400 mA $cm^{-2}$ for $KHCO_3$ and 800 mA $cm^{-2}$ for $CsHCO_3$. The changes of gas ratio by current density are well explained by the schematic illustration in Fig. 1d. The ratio of $CO_2$ and $O_2$ is close 2 in the current density region showing high faradaic efficiency (FE) for CO, indicating the main carbonate ion transfer from cathode to anode.[30,31] The decreased $CO_2$ at the anode shows transfer of hydroxide ions from the cathode, suggesting a highly alkaline reaction environment at the cathode sufficient to prevent hydroxide ion contact with $CO_2$. Additionally, as shown in the *in situ*/*operando* Raman results in Fig. 1b, the mass transfer of $CO_2$ to the catalyst layer is impeded by high local pH, further limiting the current density for $CO_2$RR. This suggests that, besides physical properties that can be improved by mechanical methods, the chemical reaction environment also plays a significant role in current limitations. Thus, chemical approaches, such as cation effects, are essential for enhancing current density in $CO_2$RR. The key for a chemical strategy is alleviating local pH by rebalancing $CO_2$ and hydroxide ion concentration at the cathode.

In nature, Earth's $CO_2$ is balanced by various carbon cycles including the carbonate-silicate cycle.[32–35] This

 This journal is © The Royal Society of Chemistry 2024

Open Access Article. Published on 30 Apuli 2024. Downloaded on 11/02/2025 23:22:28.
This article is licensed under a Creative Commons Attribution-NonCommercial 3.0 Unported Licence.

geochemical process redistributes $CO_2$ in the atmosphere to the oceans and land by rainwater, silicate weathering, carbonate precipitation and sedimentation, resulting in drawdown of atmospheric $CO_2$ (Fig. 1e) The stored $CO_2$ in land is redistributed to the atmosphere by volcanism. In this study, we aim to break the current density limitation for $CO_2$RR using silica oxide *via* a silica-hydroxide cycle, similar to the carbonate-silicate cycle. The unique silica properties allow distribution of the high $OH^-$ concentration at the catalyst surface to the other cathode side, reducing the elevated local pH at the catalyst surface and facilitating mass transfer of $CO_2$ for $CO_2$RR.

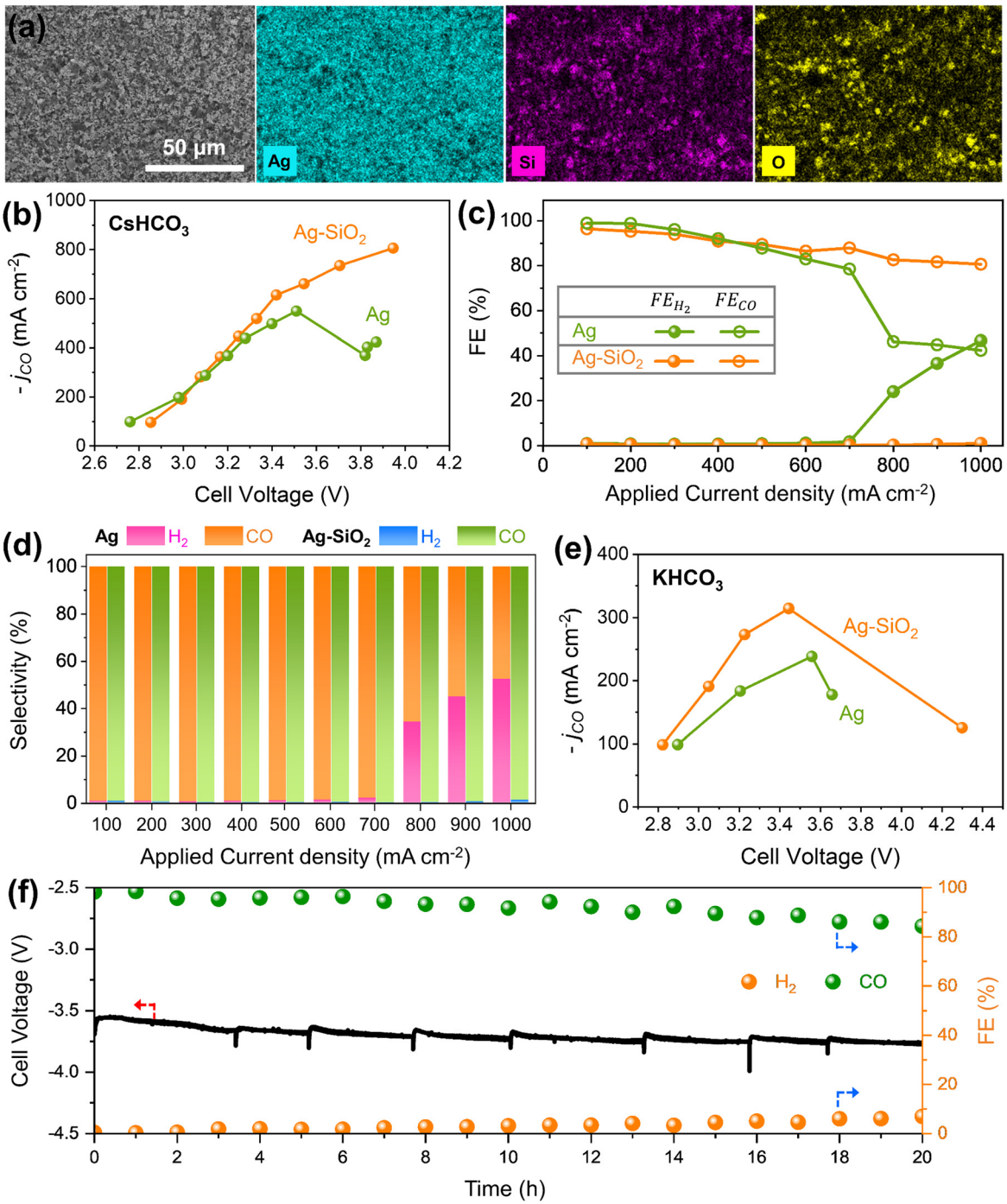


Fig. 2 Impact of $SiO_2$ in MEA $CO_2$ electrolyzer, alongside $CO_2$RR performance comparisons between Ag black and Ag–$SiO_2$. (a) SEM image and EDS elemental mapping of the Ag–$SiO_2$ electrode. (b) CO partial current density, (c) $H_2$ and CO faradaic efficiency, and (d) $H_2$ and CO selectivity for both Ag black and Ag–$SiO_2$ using 0.1 M $CsHCO_3$. (e) CO partial current density of Ag black and Ag–$SiO_2$ with 0.1 M $KHCO_3$. (f) Durability test for Ag–$SiO_2$ in the zero-gap electrolyzer using 0.1 M $CsHCO_3$ at 700 mA $cm^{-2}$ for 12 h.

Open Access Article. Published on 30 Apuli 2024. Downloaded on 11/02/2025 23:22:28.
This article is licensed under a Creative Commons Attribution-NonCommercial 3.0 Unported Licence.

## Results and discussion

### Effects of $SiO_2$ on current density for $CO_2RR$

An Ag–$SiO_2$ electrode was fabricated on a GDE by spraying ink of a mixture of $SiO_2$ nanopowder and commercial Ag black (Fig. S4–S6, ESI†). Fig. 2a illustrates SEM and SEM-EDX mapping images of the Ag–$SiO_2$ electrode, indicating that Ag black and $SiO_2$ nanoparticles are well dispersed on the GDE substrate. The effects of $SiO_2$ for $CO_2RR$ performance were studied by using an anion exchange membrane (AEM) zero-gap electrolyzer with 0.1 M $CsHCO_3$ anolyte and humidified $CO_2$ gas (Fig. 2b, d and Fig. S7, ESI†).[36,37] At an applied current density below 600 mA $cm^{-2}$, both the Ag and Ag–$SiO_2$ electrodes show similar $CO_2RR$ performance, with a high $FE_{CO}$ exceeding 90%. However, above an applied current density of 700 mA $cm^{-2}$, the $FE_{H2}$ of the Ag electrode drastically increased with rising current density, resulting in a maximum current density for CO of 549 mA $cm^{-2}$. On the other hand, the $FE_{CO}$ for the Ag–$SiO_2$ electrode remained at over 80% and the selectivity for CO ($H_2$ and CO, $SE_{CO}$) was nearly 100% at an applied current density until 1 A $cm^{-2}$ while suppressing the HER. The difference of $FE_{CO}$ and $SE_{CO}$ at a high current density region would come from production of formate (Fig. S8, ESI†). The maximum current density of the Ag–$SiO_2$ electrode for CO reached a value of 806 mA $cm^{-2}$, implying that additional $SiO_2$ to the Ag black electrode contributed to breaking the current density limitation for $CO_2RR$. Exploring the effects of varying $SiO_2$ ratios indicates the necessity for an optimal amount of $SiO_2$ (Fig. S9, ESI†). To confirm the physical effects, an Ag–$TiO_2$ electrode was fabricated using similar size of $TiO_2$ instead of $SiO_2$ (Fig. S10, ESI†). Ag–$TiO_2$ exhibits a similar limiting current density to Ag for $CO_2RR$. The results of Ag–$TiO_2$ and the comparable ECSA value for both the Ag and Ag–$SiO_2$ electrodes show that the impact of $SiO_2$ does not originate from physical properties (Fig. S11 and S12, ESI†). A similar phenomenon of breaking the maximum current density limit for $CO_2RR$ was observed using 0.1 M $KHCO_3$ anolyte at lower current densities (Fig. 2e and Fig. S13, ESI†). To validate the $SiO_2$ effects for high current density, chronopotentiometry tests were conducted at a current density of 700 mA $cm^{-2}$ where the effect of $SiO_2$ is seen (Fig. 2f and Fig. S14, ESI†). $FE_{CO}$ of the Ag electrode was close to 80% and rapidly decreased after 3 h. In contrast, the Ag–$SiO_2$ electrode demonstrated stable cell voltage and consistent $FE_{CO}$ above 90% for 12 h, suggesting that the effects of $SiO_2$ are not an instant phenomenon and could serve as a sustained strategy.

### The origin of $SiO_2$ effects in breaking current density limitation

To elucidate the origins of $SiO_2$ effects that overcome the current density limitation of $CO_2RR$, the cathode reaction

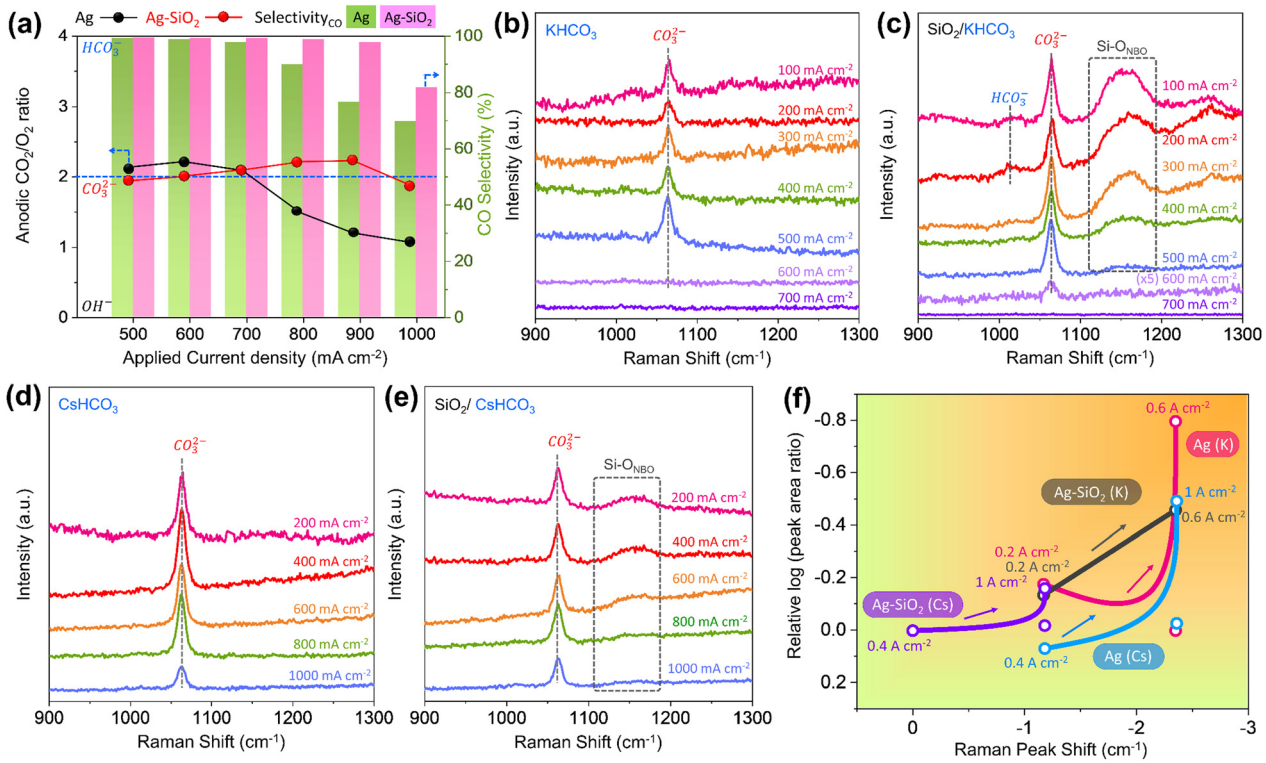


Fig. 3 The analyses of the role of $SiO_2$ in modulating the cathode reaction environment. (a) $CO_2/O_2$ ratio at the anode in a zero-gap electrolyzer using Ag–$SiO_2$ with 0.1 M $CsHCO_3$. (b) *In situ*/*operando* Raman spectroscopy results for the Ag electrode in 1 M $KHCO_3$ electrolyte. (c) *In situ*/*operando* Raman spectroscopy results for the Ag–$SiO_2$ electrode in 1 M $KHCO_3$ electrolyte. (d) *In situ*/*operando* Raman spectroscopy results for the Ag electrode in 1 M $CsHCO_3$ electrolyte. (e) *In situ*/*operando* Raman spectroscopy results for the Ag–$SiO_2$ electrode in 1 M $CsHCO_3$ electrolyte. (f) Summary of *in situ*/*operando* Raman spectroscopy results using carbonate Raman peak shifts and carbonate peak intensity ratios for both Ag and Ag–$SiO_2$ electrodes in $KHCO_3$ and $CsHCO_3$ electrolytes. Reference points for peak shift and intensity: $KHCO_3$, 100 mA $cm^{-2}$; $CsHCO_3$, 200 mA $cm^{-2}$.

 This journal is © The Royal Society of Chemistry 2024

Open Access Article. Published on 30 Apuli 2024. Downloaded on 11/02/2025 23:22:28.
This article is licensed under a Creative Commons Attribution-NonCommercial 3.0 Unported Licence.

environment in the MEA electrolyzer was investigated using gas analysis of the anode and *in situ*/*operando* Raman spectroscopy using a GDE. For the Ag–$SiO_2$ electrode, the gas composition ratio of $CO_2$ to $O_2$ remains near 2 within a current density range of 500–1000 mA $cm^{-2}$. However, for the Ag electrode, this ratio drops to almost 1 when the current density exceeds 800 mA $cm^{-2}$ (Fig. 3a). This suggests that $SiO_2$ mitigates the local pH effects stemming from high current densities.

To more directly observe the reaction environment of the cathode, *in situ*/*operando* Raman spectroscopy was carried out using a customized GDE Raman cell (Fig. S15, ESI†).[38] To estimate the pH of the cathode according to current density, we constructed two calibration curves for ranges of 9–13 and 13–14 (Fig. S16–S20, ESI†). Even at a low current density of 100 mA $cm^{-2}$, the bicarbonate peak for all *in situ*/*operando* Raman spectra nearly disappears, signifying pronounced local pH effects in the GDE.[23] In a $KHCO_3$ electrolyte, the carbonate peak disappears for the Ag electrode at a current density of 600 mA $cm^{-2}$ (Fig. 3b). Conversely, for the Ag–$SiO_2$ electrode, a minor carbonate peak persists at the same current density, indicating that $SiO_2$ mitigates local pH effects, reminiscent of cation effects (Fig. 3c). The Ag–$SiO_2$ electrode also exhibited a similar trend in $CsHCO_3$ electrolyte. The carbonate peak for the Ag electrode is lower than that for the Ag–$SiO_2$ electrode at a current density of 1 A $cm^{-2}$ (Fig. 3d and e).

For the Ag–$SiO_2$ electrode, peaks corresponding to Si–$O_{NBO}$ (where NBO is non-bridging oxygen) were observed at a current density between 100 and 400 mA $cm^{-2}$, hinting at the onset of $SiO_2$ degradation in alkaline conditions (Fig. S21, ESI†).[39,40] For intuitive representation of local pH under various conditions,

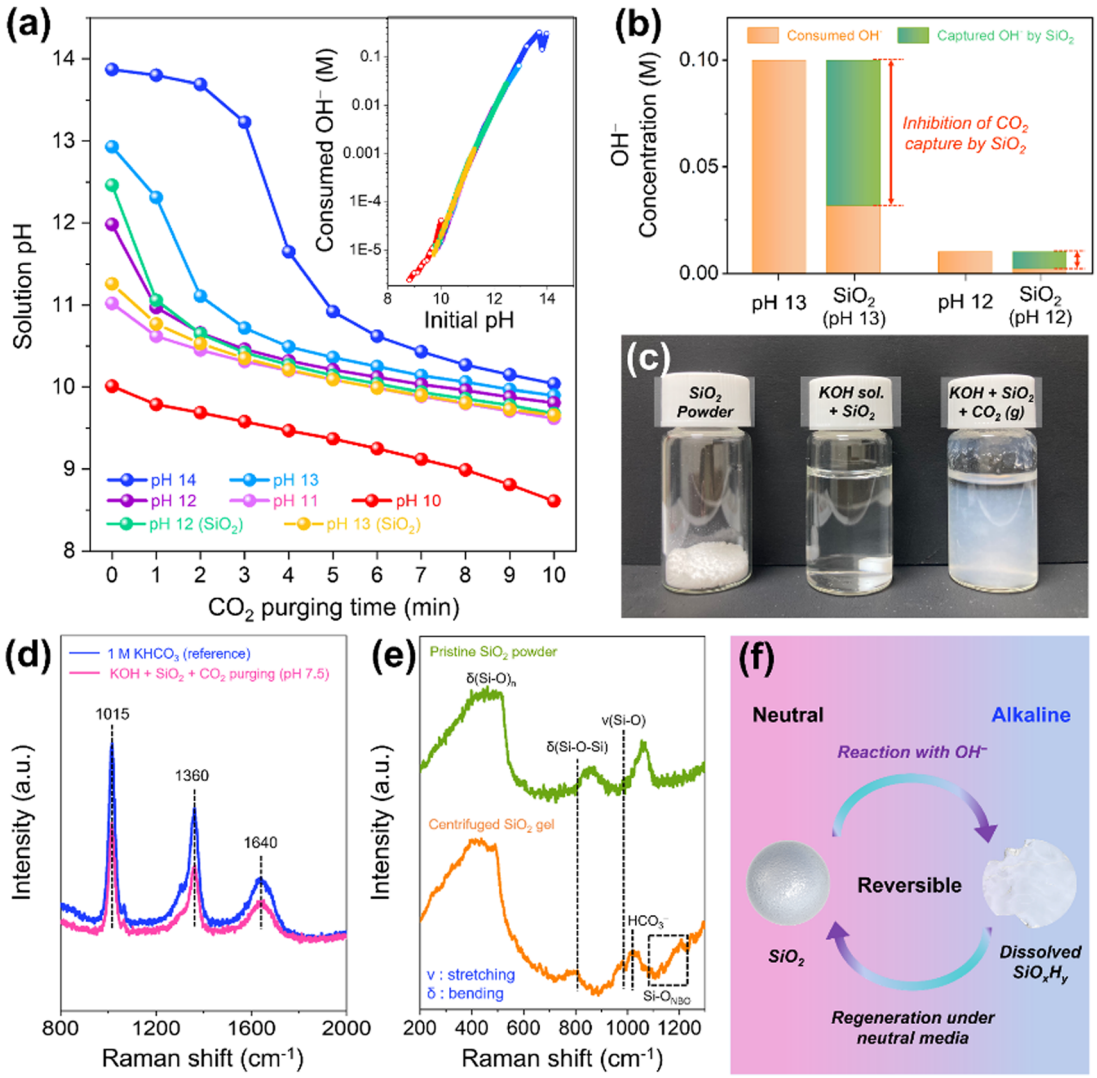


Fig. 4 Analysis of $SiO_2$ in $CO_2$RR media. (a) Change in solution pH for various initial pH solutions under $CO_2$ purge, plotted against $CO_2$ purging time (Inset: Quantity of $OH^-$ consumed based on current pH). (b) Variation in $OH^-$ concentration during $CO_2$ purging, attributed to $OH^-$ capture due to the presence of $SiO_2$. (c) Images of pristine $SiO_2$ powder, $SiO_2$-dissolved KOH solution, and an opaque gel obtained within the $SiO_2$-dissolved KOH solution after $CO_2$ purging. (d) Raman spectra comparing 1 M $KHCO_3$ solution (reference), and the $CO_2$-purged, $SiO_2$-dissolved KOH solution (containing the opaque gel). (e) Raman spectra comparing pristine $SiO_2$ powder and centrifuged $SiO_2$ gel obtained from the opaque gel within the $CO_2$-purged solution. (f) A schematic illustrating the reversible behavior of $SiO_2$ species during the reaction.

Open Access Article. Published on 30 Apuli 2024. Downloaded on 11/02/2025 23:22:28.
This article is licensed under a Creative Commons Attribution-NonCommercial 3.0 Unported Licence.

we summarize the *in situ*/*operando* Raman results based on two parameters: the log-transformed relative peak area ratio of the carbonate peak and its shift (Fig. 3f). The carbonate peak shift is expected to be related to the Stark effect or cation concentration.[41–43] However, since there is no carbonate intermediate in the $CO_2$RR mechanism on the Ag surface, we assumed that this peak shift was caused by cation concentration. The calibration results unequivocally show that carbonate peak area, which is related to carbonate concentration, is correlated to pH and peak shift corresponds to cation concentration (Fig. S22 and S23 and Note S2, ESI†). Based on calibration data, the estimated local pH results from *in situ*/*operando* Raman spectra are shown in Fig. S24 and Table S1 (ESI†). While the alkalinity of the Ag electrode increased with current density, the Ag–$SiO_2$ electrode in comparison retained its pH, underscoring the role of $SiO_2$ in the suppression of local pH effects.

### Behavior of $SiO_2$ in $CO_2$RR system

In an effort to understand the effects of $SiO_2$, it is necessary to observe the behavior of $SiO_2$ in a medium that simulates the

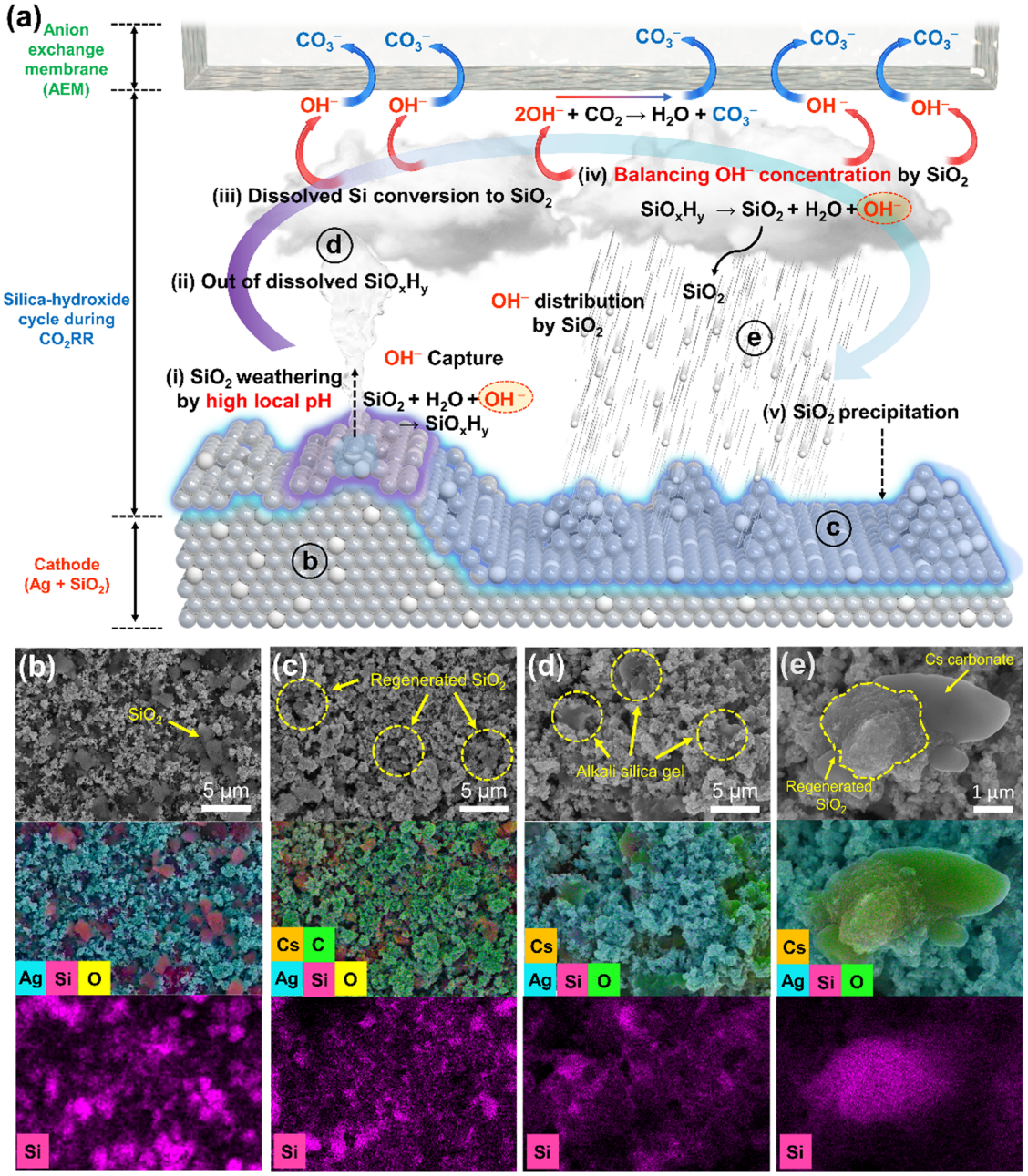


Fig. 5 Geological and spectral observations of silica-hydroxide cycle in MEA $CO_2$ electrolyzer. (a) A schematic representation of the carbonate-silicate geochemical cycle occurring during electrochemical $CO_2$ reduction reaction on Ag–$SiO_2$. SEM images and EDS elemental mapping of the Ag–$SiO_2$ electrode before (b) and after (c)–(e) reaction (c: 900 mA $cm^{-2}$ for 20 min; (d) and (e): 1 A $cm^{-2}$ for 20 min) in MEA $CO_2$ electrolyzer.

 This journal is © The Royal Society of Chemistry 2024

Open Access Article. Published on 30 Apuli 2024. Downloaded on 11/02/2025 23:22:28.
This article is licensed under a Creative Commons Attribution-NonCommercial 3.0 Unported Licence.

reaction environment for a $CO_2$ MEA electrolyzer. To verify the neutralization of local pH by $CO_2$, we purged the $CO_2$ gas into solutions of various pH and measured the pH every minute (Fig. 4a). As the duration of the $CO_2$ purge increased, the solution's pH decreased, owing to the reaction of $OH^-$ ions with $CO_2$, resulting in carbonate ions. The amount of consumed $OH^-$ with $CO_2$ is proportional to pH of solution, highlighting the alkalinity problem that blocks the transfer of $CO_2$ to active sites due to the high local pH. When the $SiO_2$ nanopowder was mixed with alkaline solution of pH 12 and 13, $SiO_2$ dissolved, leading to a decrease in the solution's pH. Regardless of the presence of $SiO_2$, the rate of $OH^-$ consumption by $CO_2$ was invariably proportional to the pH of the solution, implying that $CO_2$ gas capture by $OH^-$ is suppressed by $SiO_2$ (Fig. 4b). Interestingly, suspensions were detected in $SiO_2$-dissolved solution following an extended $CO_2$ purge (Fig. 4c). The analysis of collected solution and precipitate (by centrifugation) after 2 h of $CO_2$ purge (the pH of solution reached 7.5) demonstrates separation of $SiO_2$ and $KHCO_3$ solution,[44] suggesting almost reversible behavior of $SiO_2$ (Fig. 4d, e and Fig. S21, S25, ESI†). When the $SiO_2$ nanopowder was mixed with solutions of 0.1 M $KHCO_3$ (pH 8.65) and 1 M $KHCO_3$ (pH 8.69), the pH remained almost unchanged at 8.70 (Fig. S26, ESI†). The presumed reaction involving $SiO_2$ is depicted in Fig. 4f. In alkaline media, $SiO_2$ dissolved and converted to silicate ions by reaction of $OH^-$. These silicate ions then precipitate as $SiO_2$ under neutral conditions with release of $OH^-$ due to low solubility.[44–46] We hypothesize that this cycle involving $SiO_2$ and hydroxide also takes place in the $CO_2$ MEA electrolyzer.

### The silica-hydroxide cycle in MEA $CO_2$ electrolyzer

The mechanism of breaking the current limitation by $SiO_2$ in a $CO_2$ electrolyzer is hypothesized as being due to the reversible cycle of $SiO_2$ between alkaline and neutral media, carrying $OH^-$ ions (Fig. 5a). We postulate that this silica-hydroxide cycle decreases the local pH of the electrode surface by increasing hydroxide distribution, thereby enhancing mass transfer of $CO_2$ for $CO_2$RR. This process of silica-hydroxide cycle is similar to the silicate-carbonate cycle that maintains the $CO_2$ level in the atmosphere. When a vigorous $CO_2$RR occurs in the MEA $CO_2$ electrolyzer, the pH of catalyst surface is presumed to be that of an alkaline medium in the range of pH 11–14 by *in situ*/*operando* Raman spectroscopy. Concurrently, the pH of the AEM is expected to be neutral owing to abundant transported carbonate ions, indicating a suitable environment for the reversible silica-hydroxide cycle.

To demonstrate the silica-hydroxide cycle in the MEA $CO_2$ electrolyzer, silica weathering, evidence of the silica-hydroxide cycle, was monitored using geological and spectral observations with SEM. The pristine Ag–$SiO_2$ electrode clearly delineates the boundary between $SiO_2$ and Ag nanoparticles (Fig. 5b and Fig. S27, ESI†). After $CO_2$RR, this boundary becomes less distinct in SEM images (Fig. 5c and Fig. S28, ESI†), and this blurring intensifies as the current density increases (Fig. S29–S33, ESI†). Nevertheless, $SiO_2$ is well dispersed in the electrode, similar to before the reaction. Notably, no discernible difference in Ag nanoparticles dependent on $SiO_2$ is observed, suggesting that $SiO_2$ has no effect on the chemical state and structure of Ag (Fig. S34–S39, ESI†). These outcomes corroborate the hypothesis of silica weathering under high current densities. To further substantiate the presence of dissolved silicate ions and the regeneration of $SiO_2$, EDS mapping was employed to discern the state of $SiO_2$. When the dissolved silicate ions dried with alkali cations, hydrous alkali silica gel is formed.[47] This hydrous alkali silica gel is observed in certain regions of the electrode, signifying the presence of dissolved silicate ions (Fig. 5d and Fig. S40, ESI†). The accumulation of regenerated $SiO_2$ on the Ag electrode, the final step of the silica-hydroxide cycle, is clearly shown in Fig. 5e. $SiO_2$ appears on the Cs carbonate precipitate that is generated during or post-$CO_2$RR, implying regenerated $SiO_2$.

Under high cathodic currents, $SiO_2$ weathering is triggered by high local pH, leading to a decrease in pH by consuming $OH^-$ at the catalyst surface. The dissolved silicate ions, not reacted with $CO_2$, move to the AEM side.[48,49] The dissolved silicate ions are converted to $SiO_2$ with counterbalancing release of $OH^-$ under neutral conditions at the AEM and the converted $SiO_2$ is redistributed on the electrode. However, the silica-hydroxide cycle is not completely reversible in the MEA electrolyzer owing to the AEM, which is highly permeable to anions and cations. SEM-EDS mapping cross-section images after reaction show that the majority of $SiO_2$ remains in the cathode, but a small amount of $SiO_2$ has been moved to the AEM and anode (Fig. S41, ESI†). To eliminate the regeneration step at the AEM, 1 M KOH was used for MEA test instead of 0.1 M $CsHCO_3$ at a current density of 700 mA $cm^{-2}$. ICP-OES analysis shows that 67.6% of $SiO_2$ is preserved on the cathode with the silica-hydroxide cycle but, without the regeneration step, 5.8% of Si remained on the cathode. These results show that the regeneration step, which is critical for reversibility of the silica-hydroxide cycle, functions in a real MEA electrolyzer. This silica-hydroxide cycle reduces the concentration of $OH^-$ that captures $CO_2$, thereby enhancing mass transfer of $CO_2$ to catalyst active sites and breaking the limitation of current density.

## Conclusions

Our study introduces a novel strategy to overcome the limitation of the current density for $CO_2$RR by a chemical cycle approach, without the need for physical modification. Hydroxide ions generated from $CO_2$RR elevate the local pH. While this can enhance selectivity, it also hinders the transfer of $CO_2$ by forming carbonate ions, thus imposing a current density limitation for $CO_2$RR. Therefore, controlling the local pH is crucial for achieving a high current density. On Earth, atmospheric $CO_2$ levels are reduced *via* carbon cycles, such as the silicate-carbonate cycle. This geological carbon cycle redistributes $CO_2$ from the atmosphere to rocks through silicate weathering. Similarly, the silica-hydroxide cycle derived using

Open Access Article. Published on 30 Apuli 2024. Downloaded on 11/02/2025 23:22:28.
This article is licensed under a Creative Commons Attribution-NonCommercial 3.0 Unported Licence.

$SiO_2$ causes a reduction in the local pH of the catalyst surface in the MEA $CO_2$ electrolyzer. $SiO_2$ weathering is triggered by high local pH, and silicate ions transport the hydroxide ions near the AEM without $CO_2$ capture at the catalyst surface and reconvert to $SiO_2$. This cycle of $SiO_2$ enhances the mass transfer of $CO_2$, breaking the current density limitation for $CO_2$RR. Considering commercialization, the future goals of the silica-hydroxide cycle should be focused on enhancing the reversibility in real MEA electrolyzers. This chemical cycle strategy also observed on Earth holds a wide-ranging applicability across various systems, offering fresh insights for augmenting their efficiency and breaking their limitations.

# Experimental procedures

### Materials and chemicals

Silver nanopowder (Alfa Aesar, APS 20–40 nm, 99.9%), silicon dioxide nanopowder (Sigma-Aldrich, 10–20 nm, 99.5% trace metal basis), titanium(IV) oxide nanopowder (Sigma-Aldrich, 21 nm primary particle size (TEM), ≥99.5% trace metals), Nafion 5 wt% ionomer solution (Sigma-Aldrich), isopropanol (DAEJUNG, 99.5%), and iridium(IV) oxide (Alfa Aesar, premion, 99.99%; Ir 84.5% min) were used as received, without further purification. Carbon paper (Fuel Cell Store, Sigracet 39BB) and platinized titanium screen (Fuel Cell Store) were employed as substrates for cathodic and anodic electrodes, respectively. These substrates were cut to the desired size using a home-made punch. $KHCO_3$, which was used as the electrolyte, was procured from Sigma Aldrich (ACS reagent, >99.7%). The AEM used was sourced from Dioxide Materials (Sustainion X37-50 grade RT).

### Preparation of Ag-based electrode for cathode

The Ag black, Ag–$TiO_2$ and Ag–$SiO_2$ electrodes were fabricated by spraying catalyst ink onto a gas diffusion layer (GDL) at 70 °C. For the Ag–$SiO_2$ catalyst ink, 90 mg of commercial silver nanopowder, 15 mg of silicon dioxide nanopowder, 120 mg of Nafion ionomer solution, and 3.5 mL of isopropanol were ultrasonically mixed. Ag–$TiO_2$ catalyst ink was fabricated with same method as for Ag–$SiO_2$ catalyst ink except for adding $TiO_2$ instead of $SiO_2$. The catalyst ink for Ag black was prepared using the same method as for Ag–$SiO_2$, but without the silicon dioxide nanopowder.

### Preparation of Ir-based electrode for anode

The electrode for OER, employed as the anode, was fabricated by spraying catalyst ink onto a platinized titanium screen using a 70 °C hot plate. The catalyst ink was prepared by mixing 120 mg of commercial iridium oxide (Alfa Aesar) with 120 mg of 5 wt% Nafion ionomer solution and 4 mL of isopropanol. The electrode had an area of 10 $cm^2$, and the iridium oxide loading was set at 2 mg $cm^{-2}$.

### Single-cell electrochemical $CO_2$ reduction reaction test

MEAs were fabricated using the catalyst-coated electrode method for electrochemical reactions, and the geometric electrode area was set at 10 $cm^2$. The fabricated electrodes, along with commercial $IrO_2$-sprayed platinized titanium screen electrodes (Alfa Aesar, with a target loading of 2.0 mg $cm^{-2}$), were employed as cathodes and anodes in all single-cell tests, respectively. The AEM (Dioxide Materials, X37-50 Grade RT) underwent pretreatment in a 1 M KOH solution for 48 h and was rinsed multiple times with deionized water before use. Following this, a 0.1 M $KHCO_3$ solution, acting as the electrolyte, was introduced to the anode side *via* a pump. Concurrently, 200 sccm of humidified $CO_2$ gas at 80 °C, heated using a mantle, was introduced to the cathode side. The electrochemical tests were conducted using a VSP potentiostat (BioLogic, VMP3B-20) equipped with a booster up to 20 A. The $CO_2$RR was conducted over 18 min for each applied current density.

A gas chromatograph (GC, Agilent 7890A) was employed for product gas analysis at the GC outlet. A water trap was interposed between the GC and the cathode outlet. Argon gas (99.999%) served as the carrier gas. The GC was fitted with a flame ionization detector (FID) to detect hydrocarbons like CO, $CH_4$, and $C_2H_4$, and a thermal conductivity detector (TCD) for hydrogen ($H_2$) gas detection. A methanizer was utilized to enhance CO detection before routing to the FID. Measurements of the product gases commenced 9 min after initiation of $CO_2$RR for each current density setting. The FEs of $H_2$ and CO were computed using the following equation:

$$\mathrm{FE}_{\mathrm{product}}\,(\%) = \frac{i_{\mathrm{product}}}{i_{\mathrm{total}}} \times 100 = \frac{V_{\mathrm{product}} \times Q \times \frac{2Fp}{RT}}{i_{\mathrm{total}}} \times 100$$

where $Q$ = flow rate of the product: $F$ = faradaic constant (96 485 C $mol^{-1}$): $p$ = pressure: $T$ = room temperature (298 K): $R$ = ideal gas constant (8.314 J $mol^{-1}$ $K^{-1}$).

The partial current densities of the products were determined from the volume of a specific product, as indicated by the GC peak.

### Physical characterization

The size distribution and microstructure of the Ag black and Ag–$SiO_2$ electrodes were examined using high-resolution transmission electron microscopy (HR-TEM, Titan at 300 kV, FEI Co., USA). HR-TEM images, high-angle annular dark-field scanning transmission electron microscopy (HAADF-STEM) images, and energy-dispersive spectroscopy (EDS) mapping were performed with a Talos F200X system (FEI). Raman spectroscopy was employed to characterize various electrodes, powdered samples, and the prepared solutions, and was conducted at room temperature with a 532-nm laser (Renishaw). XPS (X-ray photoelectron spectroscopy, Nexsa, ThermoFisher Scientific) was conducted with a base pressure of $2 \times 10^{-8}$ mbar and a monochromated Al Kα (1486.6 eV) X-ray source. All XPS spectra were calibrated using the C 1s peak (284.8 eV) as a reference.

### *In situ*/*operando* Raman spectroscopy

*In situ*/*operando* SERS (surface-enhanced Raman spectroscopy) was conducted using a standard three-electrode system, a custom-made *in situ* Raman cell (details provided in Fig. S14,

 This journal is © The Royal Society of Chemistry 2024

Open Access Article. Published on 30 Apuli 2024. Downloaded on 11/02/2025 23:22:28.
This article is licensed under a Creative Commons Attribution-NonCommercial 3.0 Unported Licence.

ESI†), and a laser with a 532-nm wavelength. The working electrode was fashioned by spraying catalyst ink (containing Ag and Ag–$SiO_2$ powders) onto a GDL (Sigracet 39BB, SGL Carbon) substrate, which amplified the Raman spectrum signal. A Pt wire and Ag/AgCl (3 M NaCl) served as the counter and reference electrodes, respectively. The electrolyte was either 1 M $KHCO_3$ or 1 M $CsHCO_3$, and gaseous $CO_2$ was purged onto the working electrode at a flow rate controlled with a ball flowmeter. The electrochemical experiments were controlled using a potentiostat (CompactStat, Ivium Technologies, Eindhoven, Netherlands). The thin electrolyte layer enveloping the electrode facilitated Raman spectroscopic observation of the working electrode's surface.

## Author contributions

C. L., S. K. and J. H. S. designed/conducted the experiments, analyzed the data and wrote the manuscript. M. H. H. performed Raman analysis of Ag black and Ag–$SiO_2$. Y.-J. K. contributed to the electrochemical cell tests. K. Y. L. and J. Y. C. provided an idea for the electrochemical analysis. H.-S. O. and W. H. L. supervised the research and wrote the manuscript. All authors reviewed the manuscript.

## Conflicts of interest

There are no conflicts to declare.

## Acknowledgements

This work was supported by institutional program grants from the Korea Institute of Science and Technology (KIST) and Research Project for 'Carbon Upcycling Project for Platform Chemicals' of the National Research Foundation (NRF) funded by the Ministry of Science and ICT (grant number: 2022M3J3A1050053) and 'Carbon to X Project' (project no. 2020M3H7A1098229) through the National Research Foundation (NRF) funded by the Ministry of Science and ICT, Republic of Korea. This research was also supported by the National Research Council of Science & Technology (NST) grant by the Korean government (MSIT) (no. CAP21011-100) and National Research Foundation of Korea (NRF) grant funded by the Korean government (MSIT) (NRF-2021R1A6A3A01086623, RS-2023-00256847).

## References

1 W. H. Lee, K. Kim, J. H. Koh, D. K. Lee, D. H. Won, H.-S. Oh, U. Lee and B. K. Min, *Nano Energy*, 2023, **110**, 108373.
2 I. E. L. Stephens, K. Chan, A. Bagger, S. W. Boettcher, J. Bonin, E. Boutin, A. K. Buckley, R. Buonsanti, E. R. Cave, X. Chang, S. W. Chee, A. H. M. da Silva, P. de Luna, O. Einsle, B. Endrődi, M. Escudero-Escribano, J. V. Ferreira de Araujo, M. C. Figueiredo, C. Hahn, K. U. Hansen, S. Haussener, S. Hunegnaw, Z. Huo, Y. J. Hwang, C. Janáky, B. S. Jayathilake, F. Jiao, Z. P. Jovanov, P. Karimi, M. T. M. Koper, K. P. Kuhl, W. H. Lee, Z. Liang, X. Liu, S. Ma, M. Ma, H.-S. Oh, M. Robert, B. R. Cuenya, J. Rossmeisl, C. Roy, M. P. Ryan, E. H. Sargent, P. Sebastián-Pascual, B. Seger, L. Steier, P. Strasser, A. S. Varela, R. E. Vos, X. Wang, B. Xu, H. Yadegari and Y. Zhou, *J. Phys.: Energy*, 2022, **4**, 042003.
3 S. Jin, Z. Hao, K. Zhang, Z. Yan and J. Chen, *Angew. Chem.*, 2021, **133**, 20795–20816.
4 J. Na, B. Seo, J. Kim, C. W. Lee, H. Lee, Y. J. Hwang, B. K. Min, D. K. Lee, H.-S. Oh and U. Lee, *Nat. Commun.*, 2019, **10**, 5193.
5 M. Jouny, W. Luc and F. Jiao, *Ind. Eng. Chem. Res.*, 2018, **57**, 2165–2177.
6 L. Ge, H. Rabiee, M. Li, S. Subramanian, Y. Zheng, J. H. Lee, T. Burdyny and H. Wang, *Chem*, 2022, **8**, 663–692.
7 M. B. Ross, P. De Luna, Y. Li, C.-T. Dinh, D. Kim, P. Yang and E. H. Sargent, *Nat. Catal.*, 2019, **2**, 648–658.
8 R. I. Masel, Z. Liu, H. Yang, J. J. Kaczur, D. Carrillo, S. Ren, D. Salvatore and C. P. Berlinguette, *Nat. Nanotechnol.*, 2021, **16**, 118–128.
9 B. Endrodi, E. Kecsenovity, A. Samu, F. Darvas, R. Jones, V. Török, A. Danyi and C. Janáky, *ACS Energy Lett.*, 2019, **4**, 1770–1777.
10 D. Higgins, C. Hahn, C. Xiang, T. F. Jaramillo and A. Z. Weber, *ACS Energy Lett.*, 2019, **4**, 317–324.
11 C. M. Gabardo, A. Seifitokaldani, J. P. Edwards, C.-T. Dinh, T. Burdyny, M. G. Kibria, C. P. O'Brien, E. H. Sargent and D. Sinton, *Energy Environ. Sci.*, 2018, **11**, 2531–2539.
12 D. Wakerley, S. Lamaison, J. Wicks, A. Clemens, J. Feaster, D. Corral, S. A. Jaffer, A. Sarkar, M. Fontecave, E. B. Duoss, S. Baker, E. H. Sargent, T. F. Jaramillo and C. Hahn, *Nat. Energy*, 2022, **7**, 130–143.
13 J. Li, G. Chen, Y. Zhu, Z. Liang, A. Pei, C.-L. Wu, H. Wang, H. R. Lee, K. Liu, S. Chu and Y. Cui, *Nat. Catal.*, 2018, **1**, 592–600.
14 D. Kim, Y. Chae, U. Lee, W. Kim and D. H. Won, *Curr. Opin. Electrochem.*, 2023, **39**, 101295.
15 Y. C. Tan, W. K. Quek, B. Kim, S. Sugiarto, J. Oh and D. Kai, *ACS Energy Lett.*, 2022, **7**, 2012–2023.
16 K. Yang, R. Kas, W. A. Smith and T. Burdyny, *ACS Energy Lett.*, 2021, **6**, 33–40.
17 W. Choi, Y. Choi, E. Choi, H. Yun, W. Jung, W. H. Lee, H.-S. Oh, D. H. Won, J. Na and Y. J. Hwang, *J. Mater. Chem. A*, 2022, **10**, 10363–10372.
18 Y. Y. Birdja, E. Pérez-Gallent, M. C. Figueiredo, A. J. Göttle, F. Calle-Vallejo and M. T. M. Koper, *Nat. Energy*, 2019, **4**, 732–745.
19 B. Endrődi, A. Samu, E. Kecsenovity, T. Halmágyi, D. Sebők and C. Janáky, *Nat. Energy*, 2021, **6**, 439–448.
20 M. C. O. Monteiro, A. Mirabal, L. Jacobse, K. Doblhoff-Dier, S. C. Barton and M. T. M. Koper, *JACS Au*, 2021, **1**, 1915–1924.
21 M. Luo, Z. Wang, Y. C. Li, J. Li, F. Li, Y. Lum, D.-H. Nam, B. Chen, J. Wicks, A. Xu, T. Zhuang, W. R. Leow, X. Wang, C.-T. Dinh, Y. Wang, Y. Wang, D. Sinton and E. H. Sargent, *Nat. Commun.*, 2019, **10**, 5814.

Open Access Article. Published on 30 Apuli 2024. Downloaded on 11/02/2025 23:22:28.
This article is licensed under a Creative Commons Attribution-NonCommercial 3.0 Unported Licence.

22 N. Govindarajan, A. Xu and K. Chan, *Science*, 2022, **375**, 379–380.
23 Z. Zhang, L. Melo, R. P. Jansonius, F. Habibzadeh, E. R. Grant and C. P. Berlinguette, *ACS Energy Lett.*, 2020, **5**, 3101–3107.
24 Y. C. Tan, K. B. Lee, H. Song and J. Oh, *Joule*, 2020, **4**, 1104–1120.
25 C. Chen, Y. Li and P. Yang, *Joule*, 2021, **5**, 737–742.
26 E. W. Lees, B. A. W. Mowbray, F. G. L. Parlane and C. P. Berlinguette, *Nat. Rev. Mater.*, 2022, **7**, 55–64.
27 F. Zhang and A. C. Co, *Angew. Chem., Int. Ed.*, 2020, **59**, 1674–1681.
28 M. R. Singh, Y. Kwon, Y. Lum, J. W. Ager, III and A. T. Bell, *J. Am. Chem. Soc.*, 2016, **138**, 13006–13012.
29 S. Ringe, E. L. Clark, J. Resasco, A. Walton, B. Seger, A. T. Bell and K. Chan, *Energy Environ. Sci.*, 2019, **12**, 3001–3014.
30 G. O. Larrazábal, P. Strøm-Hansen, J. P. Heli, K. Zeiter, K. T. Therkildsen, I. Chorkendorff and B. Seger, *ACS Appl. Mater. Interfaces*, 2019, **11**, 41281–41288.
31 M. Ma, E. L. Clark, K. T. Therkildsen, S. Dalsgaard, I. Chorkendorff and B. Seger, *Energy Environ. Sci.*, 2020, **13**, 977–985.
32 R. G. Hilton and A. J. West, *Nat. Rev. Earth Environ.*, 2020, **1**, 284–299.
33 D. E. Penman, J. K. Caves Rugenstein, D. E. Ibarra and M. J. Winnick, *Earth-Sci. Rev.*, 2020, **209**, 103298.
34 A. Bufe, N. Hovius, R. Emberson, J. K. C. Rugenstein, A. Galy, H. J. Hassenruck-Gudipati and J.-M. Chang, *Nat. Geosci.*, 2021, **14**, 211–216.
35 C. S. Cockell, T. Bush, C. Bryce, S. Direito, M. Fox-Powell, J. P. Harrison, H. Lammer, H. Landenmark, J. Martin-Torres and N. Nicholson, *Astrobiology*, 2016, **16**, 89–117.
36 M. H. Han, D. Kim, S. Kim, S.-H. Yu, D. H. Won, B. K. Min, K. H. Chae, W. H. Lee and H.-S. Oh, *Adv. Energy Mater.*, 2022, **12**, 2201843.
37 W. H. Lee, Y.-J. Ko, Y. Choi, S. Y. Lee, C. H. Choi, Y. J. Hwang, B. K. Min, P. Strasser and H.-S. Oh, *Nano Energy*, 2020, **76**, 105030.
38 Y.-J. Ko, J.-Y. Kim, W. H. Lee, M. G. Kim, T.-Y. Seong, J. Park, Y. Jeong, B. K. Min, W.-S. Lee, D. K. Lee and H.-S. Oh, *Nat. Commun.*, 2022, **13**, 2205.
39 J.-L. You, G.-C. Jiang, H.-Y. Hou, H. Chen, Y.-Q. Wu and K.-D. Xu, *J. Raman Spectrosc.*, 2005, **36**, 237–249.
40 A. Osipov, L. Osipova and R. Zainullina, *Int. J. Spectrosc.*, 2015, **2015**, 572840.
41 W. W. Rudolph, D. Fischer and G. Irmer, *Appl. Spectrosc.*, 2006, **60**, 130–144.
42 Y. Ma, W. Yan, Q. Sun and X. Liu, *Geosci. Front.*, 2021, **12**, 1018–1030.
43 M. Moradzaman and G. Mul, *ChemElectroChem*, 2021, **8**, 1478–1485.
44 J. H. M. Visser, *Cem. Concr. Res.*, 2018, **105**, 18–30.
45 A. N. Palmer and M. V. Palmer, *Speleogenesis and Evolution of Karst Aquifers*, 2003, vol. **1**, pp. 1–8.
46 B. Lagerblad and J. Trägårdh, *Conceptual model for concrete long time degradation in a deep nuclear waste repository*, Swedish Nuclear Fuel and Waste Management Co., Sweden, 1994.
47 R. B. Figueira, R. Sousa, L. Coelho, M. Azenha, J. M. de Almeida, P. A. S. Jorge and C. J. R. Silva, *Constr. Build. Mater.*, 2019, **222**, 903–931.
48 S.-Y. Pan, E. Chang and P.-C. Chiang, *Aerosol Air Qual. Res.*, 2012, **12**, 770–791.
49 M. Santoro, F. Gorelli, J. Haines, O. Cambon, C. Levelut and G. Garbarino, *Proc. Natl. Acad. Sci. U. S. A.*, 2011, **108**, 7689–7692.

 This journal is © The Royal Society of Chemistry 2024